Ultra-Wideband Range Measurement Model with Gaussian Processes

Anton Ledergerber and Raffaello D'Andrea

Abstract— **This paper presents an ultra-wideband range measurement model based on Gaussian processes. An analysis of the range measurement error with off-the-shelf ultra-wideband radio modules reveals a strong correlation between the reported error and the relative pose of the two ranging modules. A Gaussian process is trained for capturing this correlation and is included in the measurement model. Its effectiveness and real-time applicability are experimentally demonstrated on a quadrocopter platform.**

I. INTRODUCTION

With its recent commercialization, the usage of ultra-wideband (UWB) radio technology for localization has gained momentum [1]. With companies such as Decawave and BeSpoon offering low-cost, low-power and small-size UWB chips, a vast range of new applications became possible. Apart from providing a communication link between two modules, the UWB technology also enables range measurement at the same time as messages are exchanged. This enables the usage of UWB technology for indoor localization.

While subcentimeter accuracies of UWB range measurements are reported in research and development [2], [3], [4], commercially available low-cost UWB systems have not yet achieved these accuracies in real-world applications. Non-line-of-sight conditions, multipath arrival times, and the influence of the UWB antenna design are just a few of the factors influencing the UWB signal propagation channel and hence also the range measured [1]. In [5], [6], the space was tessellated and each area was associated with a unique UWB measurement model to cope with non-line-of-sight conditions. Instead of modifying the localization algorithm, machine learning techniques can be used to identify and compensate for non-line-of-sight conditions when analyzing the received UWB waveform [7], [8]. The effect of angle-dependent UWB pulse distortion as well as the effect of path overlap on range accuracy are studied in [9], and a modified leading-edge detection algorithm is suggested to eliminate bias caused by path overlaps. Multiple antennas and multiple carrier frequencies are used in [10] to mitigate the effects of channel and angle-dependent range bias. Lookup tables are used in [11] to compensate for both angle-dependent and signal strength-dependent range bias.

Motivated by the systematic range error reported by [12], [13], [14], [15], who all used off-the-shelf UWB modules, this paper identifies the range error estimation as one of

The authors are with the Institute for Dynamic Systems and Control, ETH Zurich, Switzerland. The contact author is Anton Ledergerber `antonl@ethz.ch`.

the keys towards more accurate low-cost, small-size, off-the-shelf localization systems. The main contributions are the analysis of the ranging error, the suggested UWB measurement model, and an experimental evaluation. The paper is structured as follows: Section II discusses the error of range measurements obtained with off-the-shelf UWB modules. Section III suggests a framework to obtain an error model for UWB range measurements which can be used for state estimation as described in Section IV. Finally, Section V shows the experimental evaluation of the suggested UWB measurement model and its real-time application.

II. RANGE MEASUREMENT ANALYSIS

In this section the ranging error of the UWB system presented in [12] is studied to warrant the error model suggested in Section III.

A. UWB System and Setup

To measure the distance between two UWB antennas connected to a Decawave DW1000 module, the two-way ranging algorithm with repeated reply (presented in [12]) is used. Ground truth for the range measurements and the relative poses of the antennas to each other are obtained by a motion capture system. Note that these motion capture measurements are only used for purposes of analysis and training; they are not required for live operation of the trained model described in Section III and Section IV.

B. Influence of Antenna Design

For analyzing the systematic error reported by [12], [13], [14], [15], range measurements with line-of-sight conditions and no immediate antenna surroundings were taken using different antenna types in an effort to qualitatively asses their influence on the error. Two Partron Dielectric Chip antennas on DWM1000 modules [16] were placed $1.7\,\text{m}$ apart. One antenna was then rotated around its x-axis (see Fig. 1 for axis labeling), then around its z-axis while range measurements z_{range} were taken. The procedure was repeated with two BroadSpec antennas [17] connected to DW1000 modules. With $\|\mathbf{r}\|$ denoting the length of the vector $\mathbf{r}$ connecting the two antennas, Fig. 1 shows the error $e = \|\mathbf{r}\| - z_{\text{range}}$ of the range measurements over the different rotations. Clearly, the BroadSpec antenna seems to influence the signal propagation channel more evenly when it is rotated around its x-axis than the Partron antenna, which might be due to its omnidirectionality in the $y - z$ plane. However, its larger size and its low radiation gain along its x-axis also make it unsuitable for certain applications such as 3D localization for wearables. A more thorough discussion about the influence of the antennas on the UWB transmission is given in [18].

C. Influence of Antenna Surroundings and Manufacturing Differences

While line-of-sight conditions were ensured for the previous measurements, a UWB antenna used in a wearable or on a mobile robot cannot always be placed so that its immediate surrounding space is free from obstacles, and thus guarantee line-of-sight conditions for all attitudes. Additionally, manufacturing differences even for the same antenna type might also influence the signal propagation channel. Therefore, more range measurements using DWM1000 modules were taken. While one module was at a fixed place on the ground (hereafter known as anchor), the other module was attached to a quadrocopter, and range measurements over different poses of the two antennas relative to each other were taken. This procedure was then repeated using different pairs of DWM1000 modules. Fig. 3 shows measurements at selected poses for three different pairs of DWM1000 modules, representative of all measurements taken. The different DWM1000 pairs seem to have a similar error in most regions. However, in a few regions the mean of the error differs slightly, and in regions where no line-of-sight

Fig. 2. Representation of the coordinate frames used in this paper: The inertial frame I, the anchor antenna fixed frame A, the quadrocopter antenna fixed frame Q and the IMU fixed frame B. The vector from the quadrocopter antenna to the anchor antenna is denoted with r and the α, β angles denote the azimuth and the elevation angles in their respective frames.

conditions are given the error varies considerably. This is the case for $140° < \alpha_Q < 220°$ in the upper plot of Fig. 3, as these measurements required the UWB signal to traverse the quadrocopter electronics (see Fig. 2 for the variable definition and setup).

III. RANGE ERROR MODEL

As seen in the previous section, a significant factor influencing the error in range measurements is the pose of

Fig. 1. The figure shows the error of the range measurements obtained with the Partron (blue) and BroadSpec (red) antennas over different incidence angles. The setups for the measurements are illustrated on top of the plots for the Partron antennas on DWM1000 modules. Analogous setups were used for the measurements with the BroadSpec antennas connected to DW1000 modules.

Fig. 3. Range measurement errors for three different antenna pairs (blue, green, red) and over different relative poses with $\mathbf{e}_z^A = -\mathbf{e}_z^Q$ (see Fig. 2 for definitions).

the two antennas relative to each other. It was further shown that there are relative poses with non-line-of-sight conditions, resulting in strong variations of the error.

Ideally, a range error model can correctly predict the relative pose-dependent error and provide a confidence interval for its prediction such that it can be used in a Kalman filter framework. This is provided by a model based on Gaussian processes [19] presented in this section.

A. Sparse Gaussian Processes

It is computationally expensive to train a standard Gaussian process on the error and the pose of the two antennas relative to each other. In addition, the resulting model is not suitable for real-time usage on a platform with limited computational power. Finally, it would be difficult to construct a non-stationary covariance function which could capture the input-dependent confidence level of the prediction. In contrast, the sparse pseudo-input Gaussian process (SPGP) [20] is well-suited to this problem. As its authors noted, it can also model non-stationarity by changing the location of the pseudo-input points.

A complete introduction to SPGP is beyond the scope of this paper; therefore, only the necessary preliminaries for the further discussion are provided and the reader is referred to [20], [21] for more details. Assuming that the relationship between an input point $\mathbf{x}$, the process $f(\mathbf{x})$ and the observed noisy target y is given by

$$y = f(\mathbf{x}) + \varepsilon, \tag{1}$$

where ε is zero mean additive Gaussian noise with variance σ^2, an SPGP defines a posterior distribution over y_* at test location $\mathbf{x}_*$. This distribution is defined by the SPGP's pseudo-input points $\bar{X} = [\bar{\mathbf{x}}_0, \bar{\mathbf{x}}_1, \ldots, \bar{\mathbf{x}}_{M-1}]^\mathrm{T}$, its training data $X = [\mathbf{x}_0, \mathbf{x}_1, \ldots, \mathbf{x}_{N-1}]^\mathrm{T}$, $\mathbf{y} = [y_0, y_1, \ldots, y_{N-1}]^\mathrm{T}$, its mean function (which is assumed to be zero in this case), and its covariance function $k(\mathbf{x}, \mathbf{x}')$ with corresponding hyperparameters θ. In the following we denote the mean and the variance of this predicted distribution with $\mathrm{SPGP}_\mu(\mathbf{x}_*)$ and $\mathrm{SPGP}_\Sigma(\mathbf{x}_*)$, respectively.

The location of the pseudo-input points and the hyperparameters are found by maximizing the likelihood of the training data

$$\bar{X}^*, \theta^* = \underset{\bar{X}, \theta}{\arg\max}\, p(\mathbf{y}|X, \bar{X}, \theta, \sigma^2), \tag{2}$$

which tends to move the pseudo-input points to locations with low output variance. Hence, the SPGP can capture input-dependent confidence levels to a certain extent.

This is demonstrated in Fig. 4, where the predictive distribution of an SPGP trained on the data from the upper plot of Fig. 3 is shown. The angle of incidence was chosen as the input to the SPGP $x = \alpha_Q$ and the error of the range measurements was the target $y = e$. The covariance function was given by the standard periodic kernel function

$$k(x, x') = \theta_0 \exp\left[-\frac{1}{2}\left(\frac{\sin(\frac{1}{2}(\alpha_Q - \alpha_Q'))}{\theta_1} \right)^2 \right], \tag{3}$$

and the number of pseudo-input points was chosen to be $M = 15$. It is clearly visible how the SPGP can capture the lack of confidence when predicting the range measurement error without line-of-sight conditions ($140° < \alpha_Q < 220°$) by moving its pseudo-input points away from that region.

B. Suitable Covariance Functions

Assuming that the error in the range measurements, as discussed in Section II, depends on the complete relative pose of the two antennas, the input $\mathbf{x}$ to the SPGP should be a parametrization of $SE(3)$. Furthermore, the covariance function $k(\mathbf{x}, \mathbf{x}')$ should define the proximity or similarity of two such input points and is therefore of great importance [19]. However, often in self-localizing UWB anchor networks, only the positions but not the attitudes of the anchors are known. In such scenarios, an SPGP with both the robot and the anchor antenna's attitude as input cannot be used. By assuming that the anchors of such a UWB system are placed with random attitudes and that their number approaches infinity, one can show that a bias in the robot's position estimate is solely caused by its relative pose to the network. An input point $\mathbf{x}_1$ and a covariance function $k_1(\mathbf{x}_1, \mathbf{x}_1')$ not containing the anchor antenna's attitude are given by

$$\mathbf{x}_1 = {}_Q\mathbf{r} \tag{4}$$

$$k_1(\mathbf{x}_1, \mathbf{x}_1') = \theta_0 \exp\left[-\frac{1 - \frac{{}_Q\mathbf{r}^\mathrm{T}{}_Q\mathbf{r}'}{\|{}_Q\mathbf{r}\|\|{}_Q\mathbf{r}'\|}}{\theta_1} - \frac{(\|{}_Q\mathbf{r}\| - \|{}_Q\mathbf{r}'\|)^2}{\theta_2} \right], \tag{5}$$

where ${}_Q\mathbf{r}$ denotes the vector $\mathbf{r}$ from the quadrocopter antenna to the anchor antenna expressed in the quadrocopter antenna fixed coordinate frame Q (see Fig. 2). The first term in the exponent correlates with the angle between two input points, whereas the second term correlates with the difference of their magnitudes.

If the anchor antenna's attitude is also known, the input
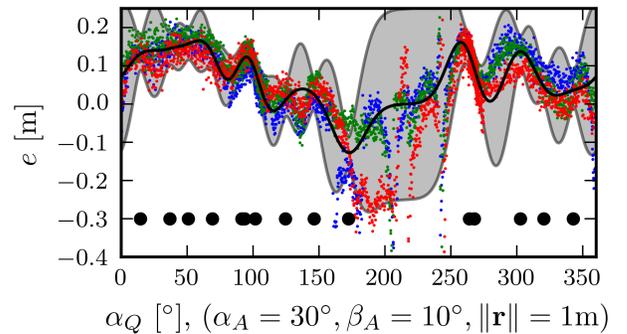
Fig. 4. The mean (black line) and twice the standard deviation (gray lines) predicted by a SPGP trained with the data shown with red, green and blue dots. The black dots show the location of the pseudo-input points after optimization.

and covariance function can be extended to

$$\mathbf{x}_2 = \begin{bmatrix} _Q\mathbf{r}^{\mathrm{T}}, _A\mathbf{r}^{\mathrm{T}} \end{bmatrix}^{\mathrm{T}} \tag{6}$$

$$k_2(\mathbf{x}_2,\mathbf{x}_2') = \theta_0 \exp \left[-\frac{2 - \frac{_Q\mathbf{r}^{\mathrm{T}}_Q\mathbf{r}'}{\|_Q\mathbf{r}\|\|_Q\mathbf{r}'\|} - \frac{_A\mathbf{r}^{\mathrm{T}}_A\mathbf{r}'}{\|_A\mathbf{r}\|\|_A\mathbf{r}'\|}}{\theta_1} \right.$$
$$\left. -\frac{(\|_Q\mathbf{r}\| - \|_Q\mathbf{r}'\|)^2}{\theta_2} \right], \tag{7}$$

where $\mathbf{x}_2$ parametrizes the relative pose of the two antennas except for the rotation around the connecting axis. For linearly polarized waves, this degree of freedom should be taken into consideration. However, including this angle did not lead to improvements and was therefore discarded. This might be due to overfitting and neglecting depolarizing effects, which in addition to the attitude of the transmitting antenna, also have an influence on the polarization [22]. SPGPs using the former and latter input points and kernel functions are hereafter denoted by SPGP$_1$ and SPGP$_2$, respectively.

IV. INTEGRATION IN A KALMAN FILTER FRAMEWORK

This section elaborates on how the SPGPs described in Section III can be used to increase the accuracy of a rigid-body Kalman filter which uses UWB range measurements and inertial measurements to update and predict its state estimate. The first-principles underlying the Kalman filter are hereby enhanced with a data-driven SPGP.

A. Prediction Equations

By taking acceleration and angular rate measurements (denoted by $\mathbf{a}$ and ω, respectively) of the inertial measurement unit as inputs to the rigid-body system, the estimated position $\mathbf{p}$, velocity $\mathbf{v}$, and orientation with respect to the inertial frame $R_{IB} \in \mathrm{SO}(3)$ evolve as follows:

$$_I\dot{\mathbf{p}} = _I\mathbf{v} \tag{8}$$
$$_I\dot{\mathbf{v}} = R_{IB}\mathbf{a} + _I\mathbf{g} \tag{9}$$
$$\dot{R}_{IB} = R_{IB}[\![\omega]\!]_\times, \tag{10}$$

where $\mathbf{g}$ is the gravitational acceleration and $[\![\omega]\!]_\times$ is the matrix form of the cross product, defined such that $[\![\omega]\!]_\times \mathbf{b} = \omega \times \mathbf{b}$ for all $\mathbf{b} \in \mathbb{R}^3$. The noise of the acceleration and angular rate measurements can be encoded as process noise using the standard Kalman filter formulation. This is a similar formulation as in [12].

B. Range Measurement Update Equation

Denoting the location of the anchor antenna with $\mathbf{p}_A$ and the position of the quadrocopter antenna with $\mathbf{p}_Q$, the range measurement is given by

$$z_{\mathrm{range}} = \|\mathbf{p}_Q - \mathbf{p}_A\| - \mathrm{SPGP}_\mu(\mathbf{x}) + \sqrt{\mathrm{SPGP}_\Sigma(\mathbf{x})}\eta, \tag{11}$$

where η is zero mean additive Gaussian noise with unit variance. Expressing $\mathbf{p}_Q$ and $\mathbf{x}$ as a function of the state variables $\mathbf{p}$ and R_{IB}, this equation can be used in a measurement update step of the rigid-body Kalman filter by means of one of the methods described in [23].

V. EXPERIMENTAL RESULTS

This section describes the implementation details and the experiments performed to assess the ranging error model and its application in a Kalman filter for a quadrocopter.

A. Implementation

The two-way ranging algorithm with repeated reply was run on the DW1000 modules such that every 5 ms a range measurement was recorded or used to update the Kalman filter, as described in Section IV. During the ranging experiments a motion capture system measured the position and attitude with an accuracy on the order of millimeters and milliradians at 200 Hz. The data hereby obtained was used to train and test the SPGPs with the GPFlow library [24]. To test the real-time applicability of the proposed method, the SPGP were reprogrammed with Eigen and run on the Snapdragon Flight computer mounted to a modified Ascending Technology Hummingbird quadrocopter. The number of inducing points was set to $M = 50$ for all experiments to keep the computational cost low, since an SPGP prediction of the mean costs $\mathcal{O}(M)$ and of the variance costs $\mathcal{O}(M^2)$ for a single test input point [20].

B. Range Error Model Evaluation

In the experiments described in Section II, range measurements over different relative antenna poses were taken. Although there was a large correlation between the error of range measurements obtained with different antenna pairs, poses of the antennas relative to each other exist in which the correlation was smaller. To quantify the effect of these local differences, SPGPs trained on different antenna pairs were applied to the same data set and the standard deviation of the remaining ranging error after correction was calculated. These numbers are shown in Table I for test data collected with the antenna pair $(0,1)$ and a standard deviation of $0.133\,\mathrm{m}$ for the range measurement error before correction $(\mathrm{stdDev}(e) = 0.133\,\mathrm{m})$. Up to 50% of the ranging error standard deviation could be explained, if the same antenna pair was used for training and for testing using a SPGP$_2$. A general antenna model trained with data from multiple antenna pairs could explain up to 35% of the standard deviation. A histogram of the original and the residual error using such a general model is shown in Fig. 5. If the SPGP represented perfectly the process $f(\mathbf{x})$ of (1), the standard deviation of the residual error should match the standard deviation of the additive process noise ε. However, the standard deviation of the process noise was calculated to be $\sigma = 0.03\,\mathrm{m}$ using static measurements. While part of the discrepancy between standard deviation of the residual error and the standard deviation of the process noise is due to model imperfections, part of it is due to the non-line-of-sight measurements accounting for about 15% of all measurements.

To analyze whether the confidence level given by an SPGP coincides with the one seen in the evaluation of the test data, all measurements with a certain confidence level in their prediction were collected in bins, and the standard

Train antenna pairs	$(0,1)$	$(2,1)$	$(2,3),(4,5)$
stdDev$(e-\text{SPGP}_{1,\mu})$ [m]	0.088	0.93	0.100
stdDev$(e-\text{SPGP}_{2,\mu})$ [m]	0.067	0.080	0.086 *

deviation of the residual measurement error after correction was calculated. Fig. 6 shows such an evaluation for the case denoted with * in Table I. As the confidence level given by the SPGP is quite accurately reflected in the data, it can be used to weight or to reject measurement data. For example, by rejecting measurement data belonging to the last two bins in Fig. 6, i.e. 12 % of the data from this experiment, the standard deviation of the residual measurement error could be reduced from 0.086 m to 0.077 m. Especially for filter initialization, when outlier rejection is more difficult, it might be of interest to consider only measurements with a high confidence level.

C. Kalman Filter Evaluation

To assess the real-world applicability of the proposed method, a range measurement model using a previously trained SPGP_1 was integrated in a Kalman filter, as outlined in Section IV. The input $\mathbf{x}_1$ to the SPGP_1 was calculated using the Kalman filter's state estimate. While the prediction step was performed using an extended Kalman filter update step, the measurement update step was performed using the spherical unscented transform [25]. A second Kalman filter not using the error model was run simultaneously for comparison. Both filters were run with 200 Hz and used the same measurements to predict and update their state estimates.

The quadrocopter was commanded to fly a circle while constantly turning around its body z-axis. During that maneuverer it received range measurements from five different

anchors, three of them were placed on the ground in a circle of radius 4 m, and two were placed at a height of approximately 2 m. Table II shows the root-mean-square error of the position estimate (denoted with $\text{RMSE}(\widehat{\mathbf{p}})$) and the standard deviations of the error before and after correction for two experiments. A reduction in the standard deviation of the range measurements seems to lead to a significant reduction of the RMSE of the position estimate. However, more experiments using different anchor placements and different commanded trajectories are needed to quantify the improvement. Fig. 7 shows the estimated positions over four flown circles. It is visible that the vertical estimation error is reduced most. This might be due to the anchor setup, which made the estimated height most sensitive to measurement errors.

Experiment	1	2
$\text{RMSE}(\widehat{\mathbf{p}})$ without error model [m]	0.22	0.19
$\text{RMSE}(\widehat{\mathbf{p}})$ with error model [m]	0.12	0.10
stdDev(e) [m]	0.13	0.13
stdDev$(e-\text{SPGP}_{1,\mu})$ [m]	0.08	0.10

VI. CONCLUSION

The ultra-wideband range measurement model presented in this paper utilizes a sparse pseudo-input Gaussian process to predict the pose-dependent error and noise level. It was demonstrated that such a measurement model can improve the localization accuracy especially in applications in which UWB antennas are placed on robots and are therefore partially shielded and strongly influenced by their surrounding.

The achievable improvements by such a measurement model strongly depend on the anchor setup, the choice of

Fig. 5. This figure compares the distribution of the ranging measurement error e (left) with the residual error after correction for the case denoted with * in Table I.
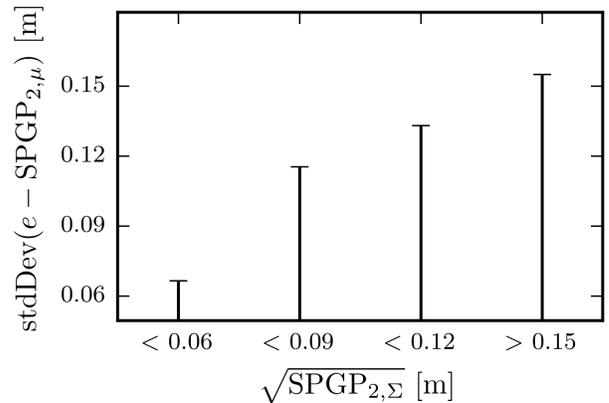
Fig. 6. The data shown in Fig. 5 and denoted with * in Table I is assigned to four different bins based on the confidence level of the error prediction. The confidence level versus the standard deviation of the residual measurement error for each bin is plotted.

covariance function, the number of pseudo-input points, the training data and the optimization routine used. A rigorous discussion of these aspects is future work.

ACKNOWLEDGMENTS

REFERENCES

[1] M. Ghavami, L. B. Michael, and R. Kohno, *Ultra Wideband Signals and Systems in Communication Engineering*. John Wiley & Sons, Feb. 2007.

[2] C. Zhang, M. Kuhn, A. E. Fathy, and M. Mahfouz, "Real-time noncoherent UWB positioning radar with millimeter range accuracy in a 3d indoor environment," in *Microwave Symposium Digest, 2009. MTT '09. IEEE MTT-S International*, Jun. 2009, pp. 1413–1416.

[3] J. C. Adams, W. Gregorwich, L. Capots, and D. Liccardo, "Ultra-wideband for navigation and communications," *Proceedings of the IEEE Aerospace Conference*, pp. 2785–2791, Mar. 2001.

[4] D. Yang, A. E. Fathy, H. Li, M. Mahfouz, and G. D. Peterson, "Millimeter accuracy UWB positioning system using sequential sub-sampler and time difference estimation algorithm," in *2010 IEEE Radio and Wireless Symposium (RWS)*, Jan. 2010, pp. 539–542.

[5] A. Prorok and A. Martinoli, "Accurate indoor localization with ultra-wideband using spatial models and collaboration," *The International Journal of Robotics Research*, pp. 547–568, Nov. 2013.

[6] D. Hoeller, A. Ledergerber, M. Hamer, and R. D'Andrea, "Augmenting ultra-wideband localization with computer vision for accurate flight," in *To appear in: Proceedings of the 20th IFAC World Congress*, 2017.

[7] H. Wymeersch, "A Machine Learning Approach to Ranging Error Mitigation for UWB Localization," *IEEE transactions on communications*, vol. 60, no. 6, pp. 1719–1728, 2012.

[8] V. Savic, E. G. Larsson, J. Ferrer-Coll, and P. Stenumgaard, "Kernel Methods for Accurate UWB-Based Ranging With Reduced Complexity," *IEEE Transactions on Wireless Communications*, vol. 15, no. 3, pp. 1783–1793, Mar. 2016.

[9] R. Ye, S. Redfield, and H. Liu, "High-precision indoor UWB localization: Technical challenges and method," in *2010 IEEE International Conference on Ultra-Wideband*, vol. 2, Sep. 2010, pp. 1–4.

[10] B. Kempke, P. Pannuto, and P. Dutta, "PolyPoint: Guiding Indoor Quadrotors with Ultra-Wideband Localization," in *Proceedings of the 2Nd International Workshop on Hot Topics in Wireless*. ACM, 2015, pp. 16–20.

[11] L. Zwirello, T. Schipper, M. Harter, and T. Zwick, "UWB Localization System for Indoor Applications: Concept, Realization and Analysis," *Journal of Electrical and Computer Engineering*, vol. 2012, p. 4, May 2012.

[12] M. W. Mueller, M. Hamer, and R. D'Andrea, "Fusing ultra-wideband range measurements with accelerometers and rate gyroscopes for quadrocopter state estimation," in *2015 IEEE International Conference on Robotics and Automation (ICRA)*, May 2015, pp. 1730–1736.

[13] J. Tiemann, F. Eckermann, and C. Wietfeld, "ATLAS - an open-source TDOA-based Ultra-wideband localization system," in *2016 International Conference on Indoor Positioning and Indoor Navigation (IPIN)*, Oct. 2016, pp. 1–6.

[14] V. Barral, P. Surez-Casal, C. J. Escudero, and J. A. Garca-Naya, "Assessment of UWB Ranging Bias in Multipath Environments." [Online]. Available: http://www3.uah.es/ipin2016/usb/app/descargas/191_WIP.pdf

[15] K. Caluwaerts, J. Bruce, J. M. Friesen, and V. SunSpiral, "State estimation for tensegrity robots," in *2016 IEEE International Conference on Robotics and Automation (ICRA)*, May 2016, pp. 1860–1865.

[16] "Decawave DWM1000 Datasheet." [Online]. Available: www.decawave.com

[17] "Broadspec Antenna." [Online]. Available: http://www.timedomain.com/datasheets/TD_Broadspec_Antenna.pdf

[18] W. Srgel and W. Wiesbeck, "Influence of the Antennas on the Ultra-Wideband Transmission," *EURASIP Journal on Advances in Signal Processing*, vol. 2005, no. 3, pp. 296–305, Mar. 2005.

[19] C. E. Rasmussen and C. K. I. Williams, *Gaussian Processes for Machine Learning*. MIT Press, 2006.

[20] E. Snelson and Z. Ghahramani, "Sparse Gaussian Processes using Pseudo-inputs," in *Advances in Neural Information Processing Systems 18*. MIT Press, 2006, pp. 1257–1264.

[21] J. Quionero-Candela and C. E. Rasmussen, "A Unifying View of Sparse Approximate Gaussian Process Regression," *Journal of Machine Learning Research*, vol. 6, pp. 1939–1959, Dec. 2005.

[22] John L. Volakis, *Antenna engineering handbook*. McGraw-Hill, 2007.

[23] J. Ko and D. Fox, "GP-BayesFilters: Bayesian filtering using Gaussian process prediction and observation models," *Autonomous Robots*, vol. 27, no. 1, pp. 75–90, Jul. 2009.

[24] A. G. d. G. Matthews, M. van der Wilk, T. Nickson, K. Fujii, A. Boukouvalas, P. León-Villagrá, Z. Ghahramani, and J. Hensman, "GPflow: A Gaussian process library using TensorFlow," *arXiv preprint 1610.08733*, Oct. 2016.

[25] S. J. Julier, "The spherical simplex unscented transformation," in *Proceedings of the 2003 American Control Conference, 2003.*, vol. 3, Jun. 2003, pp. 2430–2434 vol.3.

Fig. 7. The top plot shows the estimated position using an error model in dashed green, the estimated position without using an error model in dotted blue and the position measured by the motion capture system in solid red. The bottom three plots show the error of the position estimates for each axis over time (dashed green: with error model, dotted blue: without error model).